

## MICROBOTICS

# Robotically controlled microprey to resolve initial attack modes preceding phagocytosis

Simone Schuerle,<sup>1,2\*</sup> Ima Avalos Vizcarra,<sup>3\*</sup> Jens Moeller,<sup>3</sup> Mahmut Selman Sakar,<sup>4</sup> Berna Özkale,<sup>5</sup> André Machado Lindo,<sup>5,6</sup> Fajer Mushtaq,<sup>5</sup> Ingmar Schoen,<sup>3</sup> Salvador Pané,<sup>5</sup> Viola Vogel,<sup>3†</sup> Bradley J. Nelson<sup>5†</sup>

2017 © The Authors, some rights reserved; exclusive licensee American Association for the Advancement of Science.

Phagocytes, predatory cells of the immune system, continuously probe their cellular microenvironment on the hunt for invaders. This requires prey recognition followed by the formation of physical contacts sufficiently stable for pickup. Although immune cells must apply physical forces to pick up their microbial prey, little is known about their hunting behavior preceding phagocytosis because of a lack of appropriate technologies. To study phagocyte hunting behavior in which the adhesive bonds by which the prey holds on to surfaces must be broken, we exploited the use of microbotic probes to mimic bacteria. We simulate different hunting scenarios by confronting single macrophages with prey-mimicking micromagnets using a 5-degree of freedom magnetic tweezers system (5D-MTS). The energy landscape that guided the translational and rotational movement of these microparticles was dynamically adjusted to explore how translational and rotational resistive forces regulate the modes of macrophage attacks. For translational resistive prey, distinct push-pull attacks were observed. For rod-shaped, nonresistive prey, which mimic free-floating pathogens, cells co-aligned their prey with their long axis to facilitate pickup. Increasing the rotational trap stiffness to mimic resistive or surface-bound prey disrupts this realignment process. At stiffness levels on the order of  $10^5$  piconewton nanometer radian<sup>-1</sup>, macrophages failed to realign their prey, inhibiting uptake. Our 5D-MTS was used as a proof-of-concept study to probe the translational and rotational attack modes of phagocytes with high spatial and temporal resolution, although the system can also be used for a variety of other mechanobiology studies at length scales ranging from single cells to organ-on-a-chip devices.

## INTRODUCTION

Population dynamics in animal ecology are directly affected by predator-prey interactions (1). Hunting behavior and relevant cues in sensing, attack, and prey capture have been well studied in macroscopic biological organisms. Similar scenarios occur in the immune host defense at the microscale. Phagocytes, predatory immune cells including macrophages, sense biochemical and physical cues of their microenvironment (2–4) to capture foreign bodies and degrade them within the phagolysosomes. The phagocytic process can be described by an initial recognition that is followed by capture, which often requires that the adhesive bonds by which prey holds on to surfaces are broken, and finally prey engulfment (5–7).

To study the underlying dynamics and mechanics of phagocytosis by mimicking such predator-prey scenarios at the cellular level, dexterous control of engineered microprobes is required. However, the required level of probe manipulation has remained challenging because of limitations in control and compatibility with the experimental requirements. For complex rotational maneuvers during cell-prey encounters, a system that detects and controls both translational and rotational motion is required. Most phagocytic studies have been conducted using spherical probes, and only limited control of both the three-dimensional (3D)

translational and rotational displacement of arbitrarily shaped particles has been shown (8–11). Although target shape largely affects the kinetics of phagocytosis (12, 13), the torques involved during the uptake of nonspherical particles have received little attention because of limitations in decoupling translational and rotational modes of cellular forces. Particle rotation was recently monitored using fluorescent tracers on beads (11, 14); however, it remains challenging to extract rotational information from spherical probes. Alternatively, optical wrenches, in combination with cylindrical quartz probes, have been used for direct rotational readout. However, this system could not decouple torque and force, was limited to a small selection of appropriate probes, and caused photo damage and sample heating (15–18).

Here, we resolve both translational and rotational dynamics during prey capture, which precedes phagocytic capture, by exploiting a 5-degree of freedom magnetic tweezers system (5D-MTS) in combination with nonspherical, micrometer-sized magnetic prey obtained using 3D-printed templates. Our system provides unconstrained control of the position and orientation of arbitrarily shaped particles, enabling twisting experiments in 3D under dynamic or constant force and torque. Customized particles were fabricated using two-photon photolithography templates followed by electrodeposition of magnetic materials. By dynamically adjusting the rotational and translational trapping stiffness, this artificial prey can mimic both, either adherent or free-floating pathogens and foreign particles. The cellular dynamics, including forces, within the initial steps of phagocytosis of mechanical resistive and nonresistive artificial prey were monitored from the initial contact by the macrophage to subsequent inward pulling. The rotational dynamics and torques exerted by cells to facilitate the pickup of nonspherical particles could also be resolved with orientation clamp measurements coupled to live actin cytoskeletal recordings. With its large working distance, the 5D-MTS can be used for a variety of other mechanobiology studies at length scales ranging from single cells to engineered tissues and organs integrated in lab-on-a-chip devices and bioreactors.

<sup>1</sup>Koch Institute for Integrative Cancer Research, Massachusetts Institute of Technology, Cambridge, MA 02139, USA. <sup>2</sup>Harvard-MIT Division of Health Sciences and Technology, Institute for Medical Engineering and Science, Massachusetts Institute of Technology, Cambridge, MA 02139, USA. <sup>3</sup>Laboratory of Applied Mechanobiology, Department of Health Sciences and Technology Zürich (ETH Zurich), CH-8092 Zurich, Switzerland. <sup>4</sup>Institute of Mechanical Engineering, École Polytechnique Fédérale de Lausanne, Station 9, CH-1015 Lausanne, Switzerland. <sup>5</sup>Institute of Robotics and Intelligent Systems, ETH Zurich, CH-8092 Zurich, Switzerland. <sup>6</sup>Instituto de Ciências Biomédicas Abel Salazar da Universidade do Porto, 4099-003 Porto, Portugal.

\*These authors contributed equally to this work.

†Corresponding author. Email: viola.vogel@hest.ethz.ch (V.V.); bnelson@ethz.ch (B.J.N.)

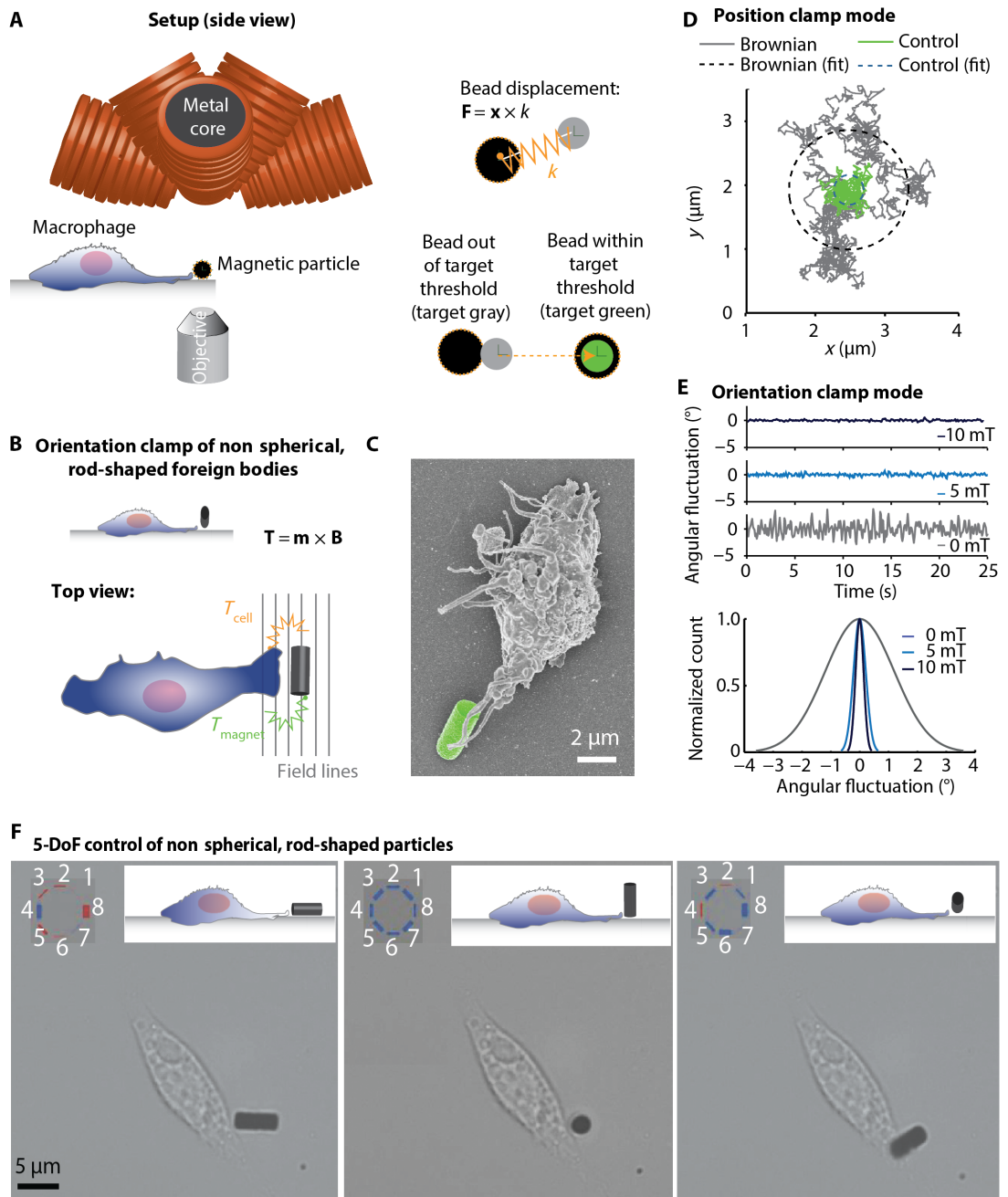
**RESULTS**
**Mimicking cellular predator scenarios**

Phagocytes in their natural habitat are often confronted with planktonic and sessile prey. Whereas planktonic pathogens and floating foreign particles can be reoriented freely, adherent prey, that is, pathogens bound to (implant) surfaces or within a surface biofilm, can resist translational or

rotational modes when attacked by immune cells (19). To resolve the cellular forces involved in the early stages of phagocytosis for adherent and nonadherent prey, we first studied the events preceding internalization of free-floating and thus nonresistive magnetic particles. Then, to mimic the behavior of surface-bound prey where macrophages have to apply force to break clusters of adhesive bonds by which bacteria adhere to the surface,

**Fig. 1. Dynamic translational and rotational resistance control of magnetic microparticles using a magnetic tweezers system (5D-MTS) to study the mechanical response of macrophages during phagocytic decision-making.**

**(A)** Schematic side view of the MTS. The eight electromagnetic coils are located above the sample stage of an inverted microscope. Right: In translational resistance control, the magnetic particle is tracked using a Canny edge detection algorithm. The orange dotted line marks the detected particle edges and is used for the evaluation of the tracking performance. After the positioning of the bead, a circular target with a radius of  $2\ \mu\text{m}$  was defined, which corresponded to less than half the size of the probe. The algorithm considers the spatial target position as reached if the centroid of the trapped particle is localized within this region.  $\mathbf{F}$  is the force vector;  $\mathbf{x}$ , distance vector. **(B)** Magnetic torque wrench concept to clamp the particle orientation. The long axis of the rod-like particle is aligned with the magnetic field direction. The particle is free to translate but is locked in its rotational degree of freedom.  $\mathbf{T}$ , torque;  $\mathbf{m}$ , magnetic moment (in  $\text{A m}^{-2}$ );  $\mathbf{B}$ , applied magnet's field flux density (in T). **(C)** SEM image of a macrophage-prey encounter. **(D)** Translational resistance performance measurements. Without macrophage contact, the position of a freely suspended microparticle is predominantly determined by Brownian motion. The Brownian motion-driven displacement of a single spherical particle is shown for a recorded time of 1 min (gray trace). By applying closed-loop position control (green trace), the mean deviation of the particle from a predetermined target position was reduced to  $220\ \text{nm}$  by applying a translational clamp stiffness of  $0.7 \times 10^{-4}\ \text{pN nm}^{-1}$  (text S3). **(E)** Orientation clamp calibration. Angular deviation under magnetically attenuated Brownian motion determined by the difference of the rod orientation between two adjacent time frames at 0-, 5-, and 10-mT externally applied magnetic field. Bottom: Corresponding Gaussian fit over normalized count of the angular deviations over time for 0, 5, and 10 mT, respectively (text S4 and figs. S9 and S10). **(F)** Five-degree of freedom (DoF) control: three snapshots of arbitrary orientations of a CoNi microrod in 3D (see also movie S1). In close vicinity to the macrophage, the microrod 3D position and orientation were controlled with respect to the cell axis. The insets depict schematic side views of the corresponding particle orientation and position. The distribution of the input current for each of the eight electromagnets is shown in the upper left corner of every micrograph, with the thickness of the bars being proportional to the magnitude of the current of each respective coil, whereas blue and red represent positive and negative signals, respectively.



we applied dynamic resistive translational or rotational forces to our “resistive prey” to counteract the forces and torques that macrophages generate to pull off the prey. Notably, flagellated bacteria typically lose their flagellum during the early phases of bio-film formation, which motivates the characteristics of our experimental scenarios. The prey, that is, commercially available magnetic microbeads or 3D-print-based microprobes (figs. S1 to S3), were coated with an anti-*Escherichia coli* immunoglobulin G (IgG) antibody or with type 1 fimbriae of *E. coli*, which expose the bacterial adhesin FimH at their tips. Scanning electron microscopy (SEM) of fixed cells after exposure to these particles revealed that macrophages internalized them, which supports their use as artificial prey (see fig. S4). With our 5D-MTS (fig. S4), a particle was placed in a target position in front of the leading edge of the cell membrane under computer vision-based closed-loop control (Fig. 1A). An in-depth description of the system and calibration can be found in text S1, as well as in previous publications (20, 21). The particle position was tracked in real time using an edge detection algorithm (text S2). When the cell exerted force on the particle, the particle was displaced from the target position, and an opposing magnetic force was automatically applied by the 5D-MTS to resist the deviation. A proportional-integral controller was implemented such that the proportional gain, and thus the strength of resistance to counteract cellular attacks, could be dynamically adjusted (see text S3). The vision-based active control system varies the energy landscape through which the movement of the magnet is confined; it creates a dynamic position clamp that allows deviation under increased resistance. The resulting translational stiffness  $k_{\text{trans}}$  was either set to zero ( $k_{\text{trans}} = 0$ ) to simulate nonresistive prey that is freely floating in the cell proximity or dynamically adjusted to mimic prey bound to tissue or biomaterial surfaces with  $k_{\text{trans}} > 0$  (Fig. 1B). Using shape-anisotropic cobalt-nickel microrods mimicking rotationally resistive prey, we additionally probed the rotational maneuvers during cell encounters (Fig. 1, C and D). The particle was free to translate, and a torque was applied and dynamically adjusted to resist reorientation of the prey during cellular maneuvers. This allowed us to resolve ranges of applied torque at which prey could survive an attack, that is, where particles were not taken up as indicated by decreased or halting rotational and translational displacement of the prey. The rotational clamp stiffness was modeled and calibrated by measuring the dependence of angular fluctuations under the applied magnetic torque, yielding a rotational trapping stiffness on the order of  $k_{\text{rot}} = 10^2$  pN nm rad<sup>-1</sup>

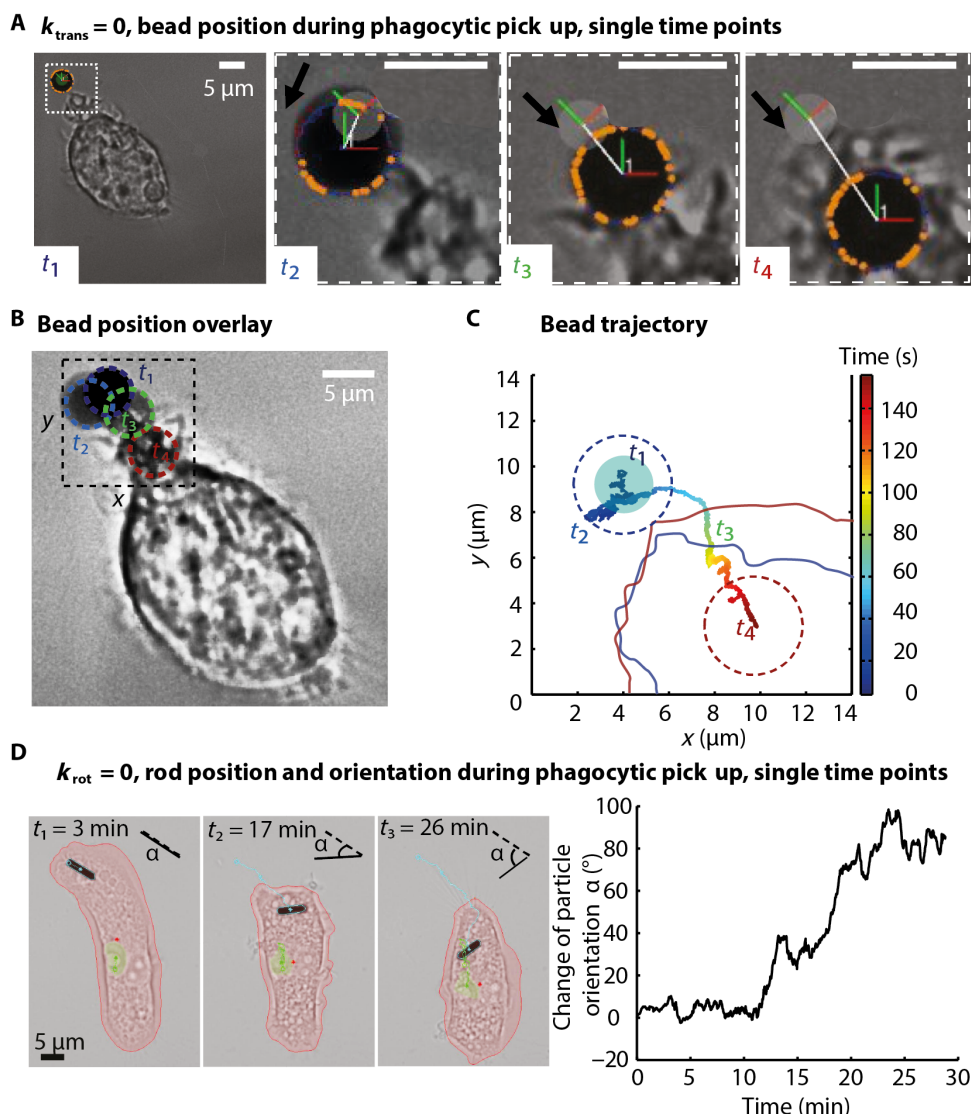


**Fig. 2. Mimicking nonresistive prey: Macrophages apply sideways push-pull maneuvers during first contact.**

(A) A freely suspended magnetic bead functionalized with IgG, which targets the Fc receptors on macrophages, was placed in close proximity to the leading edge of a surface-adherent macrophage. Once the bead reached its target position, magnetic control was switched off to observe undisturbed cellular pickup kinetics. Right: Three enlarged insets of the region of interest (white) at distinct time points (see also movies S3 and S4). (B) Overlay of four time points during this push-pull sequence, demonstrating the curved trajectory. (C) Plot of the bead position over time in the region of interest (black). The colored trajectory depicts the motion of the free-floating bead, shortly before the first cellular contact ( $t_1$ ), followed by a sideways push ( $t_2$ ) with subsequent pull toward the cell body ( $t_3$ ) until pickup is completed ( $t_4$ ). Blue and red lines depict cell outlines at  $t_1$  and  $t_4$ , respectively. (D) Sequence of a macrophage maneuvering an elongated, nonresistive microprey. The microrod was rotated by the cell by the angle  $\alpha = 90^\circ$  from its initial orientation (dotted line), as shown in the plot on the right. The cell outline was tracked (red line) and used to compute the cell center (red dot) and shows how the distance to rod position (cyan) is decreasing. The motion of the nucleus (green) is plotted (see also movie S5).

for the given probes (see Fig. 1E and text S4). In summary, our 5D-MTS allowed us to present artificial microprey to surface-adhering cells in user-defined orientations in 3D under dynamic resistance by applying defined magnetic torques (Fig. 1F and movies S1 and S2).

### Nonresistive phagocytic targets are first pushed by macrophages, followed by a curved pickup pull

Anti-*E. coli* IgG functionalized microbeads that mimicked free-floating, nonresistive prey were placed close to the cell leading edge. The switch

between screening and engulfment (22) was recorded in real time by tracking the cell motion and bead trajectory at an applied translational stiffness of zero, that is,  $k_{\text{trans}} = 0$ . When following a single macrophage over time (Fig. 2, A to C), distinct directional changes of the prey during the first moments of contact could be observed. Soon after initial contact, the bead was pushed aside (phase 1, Fig. 2, A to C;  $t_1$  to  $t_2$ ) before it was pulled toward the cell body in a characteristic curved or C-shaped trajectory (phase 2, Fig. 2, A to C;  $t_2$  to  $t_3$ ). The push velocity in this early encounter increased up to 670 nm/s (mean of 95th percentile), resulting in a displacement of 1.4  $\mu\text{m}$ , after which the cell pulled on the bead with a mean velocity of  $170 \pm 85 \text{ nm s}^{-1}$ , as measured along the curved trajectory, until pickup (Fig. 2, A to C;  $t_2$  to  $t_3$ ). The bead path was monitored until the cell had picked up its prey to transport it on the membrane toward the cell center (movies S3 and S4). Such bead movement on the upper side of the plasma membrane of cells had previously been described in optical tweezers experiments, with average velocities of  $110 \text{ nm s}^{-1}$  (23).

Although it is well documented that surface-adhering phagocytic cells pull on objects, our finding that pulling is typically preceded by pushing has not been previously reported to the best of our knowledge. Throughout the multistep process, actin plays a key role in driving cellular dynamics through spatiotemporal reorganization of the cytoskeleton to contact and eventually engulf the prey. During initial contact, continuous dynamic probing by cell membrane protrusions and by the formation of a sufficient number of adhesive bonds is required for efficient prey capture (24). The observed initial pushing requires that the macrophages contact their prey by actively polymerizing actin-rich protrusions and agrees with existing literature (22–26).

### Nonresistive, elongated phagocytic prey is rotated during pickup to align with the long cell axis

The morphology and aspect ratio of the prey is an important parameter that controls the rate of phagocytosis. Macrophages tend to engulf high-aspect ratio pathogens or foreign particles by forming a phagocytic cup around the terminal pole of the prey or abort phagocytosis if this is not possible (12, 13, 27–29). Immune cells can thus recognize the shape of their prey, and if they contact just the long axis, phagocytosis is inhibited. Although previous optical and magnetic trapping experiments used spherical beads, the ability to trap arbitrary-shaped microparticles allows for the investigation of how particle shape affects cellular forces and the uptake rate, as well as the direct readout of cellular rotational maneuvers. Control of nanowires in 3D has recently been reported using multiple beam optical traps, but manipulation control is limited and the systems have not been applied to quantify cellular forces (30, 31). When non-spherical, nonresistive prey was presented to cells, rotational maneuvers were observed to align and transport the prey toward the cell body (Fig.

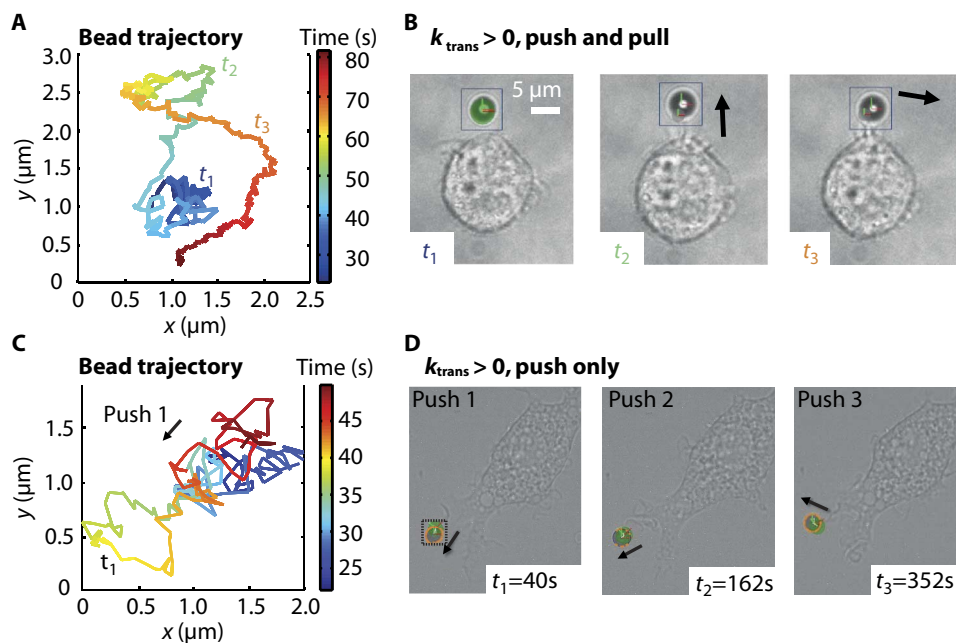


**Fig. 3. Push-pull versus push without follow-up pickup events.** (A and B) Experiment with an anti-*E. coli* antibody functionalized bead (see also fig. S7 and movie S7). (A) Bead trajectory over the course of the initial cell contact. (B) Corresponding micrographs at distinct time points  $t_1$  to  $t_3$ , illustrating the dynamics during particle pickup. The spherical particle was placed in close proximity to the cell (green target position at  $t_1$ ). Membrane protrusions toward the particle pushed the bead upward away from the cell body for about 20 s. The deviation-dependent applied resistive force reached up to 0.35 pN at  $t_2$  (fig. S7). Afterward, the motion was reversed and the bead was pulled sideways toward the cell body, resulting in a characteristic C-shaped trajectory. (C and D) Experiment with a FimH-type I fimbriae-coated bead (see also fig. S9). (C) Trajectory of a push-only sequence corresponding to the image at  $t_1 = 40$  s within the black square. The bead is pushed away by the cell, but no pickup pull follows; instead, the bead is recovered into its original position through the applied control loop of the 5D-MTS. At two distinct time points later, the cell pushed again, as depicted in (D); however, in both cases, again no further pickup pull toward the cell body followed, and the bead eventually remained in its original target position.

2D and movie S5). Increased vacuole activity, including fusion and motility, was seen along the edges of the microrods (Fig. 2D;  $t_1$  to  $t_2$ ). The cell rotated the microprey by about  $90^\circ$  and initiated the uptake of the rod-shaped target at one pole, as indicated by focal plane changes across the cell body and shortening of the projected microrod length. This behavior was repeatedly observed for parallel and antiparallel initial alignment of the rods and the cell axis (see also movie S6), supporting earlier findings that local particle shape, in addition to size, influences the kinetics and efficiency of particle uptake (12, 27, 29, 32).

### Detailed dynamics of initial push maneuvers are indicative of subsequent successful prey pickup

Next, the initial pushing maneuvers observed for nonresistive particles were investigated for prey being held in the target position by applying small counteracting forces through an automated visual feedback loop. The applied counteracting magnetic force linearly increases with the distance of the particle from the target position, at a slope determined by the applied spring constant ( $k_{\text{trans,max}} = 1.8 \times 10^{-4} \text{ pN nm}^{-1}$ ; see text S3). This results in the microprey giving resistance against being pushed by its predator.

To study whether the hunting behavior is dependent on the surface chemistry displayed by the beads, we coated the beads with either an anti-*E. coli* IgG antibody or the bacterial type I fimbriae, thus addressing two different types of membrane receptors. Among the 27 experiments simulating resistive prey ( $k_{\text{trans}} > 0$ ), two subgroups with different dynamics were identified, that is, pushing with or without a subsequent pull sequence (see fig. S6). The “push-only” behavior was dominantly

found for fimbriae-coated particles (12 of 13 experiments). The bacterial adhesin FimH is found at the tip of *E. coli*'s type 1 fimbriae and is specifically recognized by the mannosylated receptor CD48, which is localized on the outer membrane of macrophages (33, 34).

In the “push-pull” scenario depicted in Fig. 3 (A and B), an anti-*E. coli* IgG functionalized microbead was placed in proximity to the cell edge, its position was tracked, and forces in the range of hundreds of femtonewtons were applied to maintain the particle position and resist Brownian and fluid-induced fluctuations. Upon first contact, the bead was pushed away from the cell edge (Fig. 3A,  $t_2$ ), yielding a linear increase of subpiconewton magnetic restoring force toward the cell that weakly counteracted this push (fig. S7A and movie S7). The prey could thus still be moved; however, the cell encountered resistive forces during this push, and the prey was moved at velocities reaching up to  $580 \text{ nm s}^{-1}$  at  $t_2$  (fig. S7B). Next, the direction of the motion was reversed, as the bead was pushed sideways (Fig. 3, A and B,  $t_2$  to  $t_3$ ). At a displacement of about  $2 \mu\text{m}$  relative to the position of first contact and an opposing force of  $0.6 \text{ pN}$  at  $t_2$  (fig. S7B), the bead was pulled toward the cell with a mean velocity of  $230 \pm 100 \text{ nm s}^{-1}$ . As depicted in Fig. 3 (A and B), this push-pull motion did not occur along a straight trajectory. Instead, the pull followed again a curved path, as also seen for nonresistive prey (Fig. 2). Such curved trajectories were recorded independently of ligand type and trap stiffness (see also fig. S8). A push-only event representing the second category of cell-prey encounter without follow-up pull is depicted in Fig. 3 (C and D). A fimbriae-coated bead was presented at the leading edge of the cell, and the bead position was clamped. Facilitated by either lamellipodia or thick, long filopodia-like spikes and membrane ruffles, the bead was pushed out of its target position during several pushes, each lasting 10 to 30 s, which was observed over a total time interval of several minutes (Fig. 3C and fig. S9). The straight push motion is reflected in the bead trajectory, as shown in Fig. 3D for the push sequence at  $t_1$ .

Taking all observations together, the first interaction between the macrophage and the bead, that is, their prey, typically resulted in a bead displacement away from the cell. This was observed for experiments with ( $k_{\text{trans}} > 0$ ) and without ( $k_{\text{trans}} = 0$ ) position clamp (Fig. 4A). In 19 experiments with free-floating, nonresistive prey ( $k_{\text{trans}} = 0$ ), cell-induced pushing velocities of  $450 \pm 250 \text{ nm s}^{-1}$  were recorded, which is substantially larger than bead displacement velocities of  $230 \pm 50 \text{ nm s}^{-1}$  for motion induced solely by Brownian and fluidic drift forces (Fig. 4B). After the push, the cell-bound, nonresistive beads are pulled toward the cell with a velocity of  $240 \pm 120 \text{ nm s}^{-1}$ . For all experiments, the change from pushing to pulling motion was determined by analyzing the trajectory with respect to changes of the bead direction away and toward the cell (figs. S6 and S8). In cases of cell encounters with resistive prey ( $k_{\text{trans}} > 0$ ) and follow-up pull, smaller pushing velocities of  $380 \pm 150 \text{ nm s}^{-1}$  were observed, which might be explained by the apparent resistance of the beads to displacement slowing down the process (Fig. 4C). Pushing without subsequent pickup (beads could be removed from the cell within 15 min after the first contact) was observed in 13 of 27 position-clamp experiments with both anti-*E. coli* antibody and fimbriae functionalized beads. In these cases, although the prey is resistive, we determined higher pushing velocities of  $480 \pm 100 \text{ nm s}^{-1}$ , with peaks up to  $2.1 \mu\text{m s}^{-1}$ . As noted earlier, this behavior, that is, push only, was dominantly observed for fimbriae-coated particles (12 of 13 experiments). We hypothesize that a lower binding yield, as compared with antibody-coated beads, might have led to failure to pick up the prey because of a sparser distribution of receptors. Among nonresistive and resistive prey, pushing velocities were statistically significantly higher ( $P < 0.05$ ) than pulling velocities, which might partially be explained by the fact that the prey got immobilized

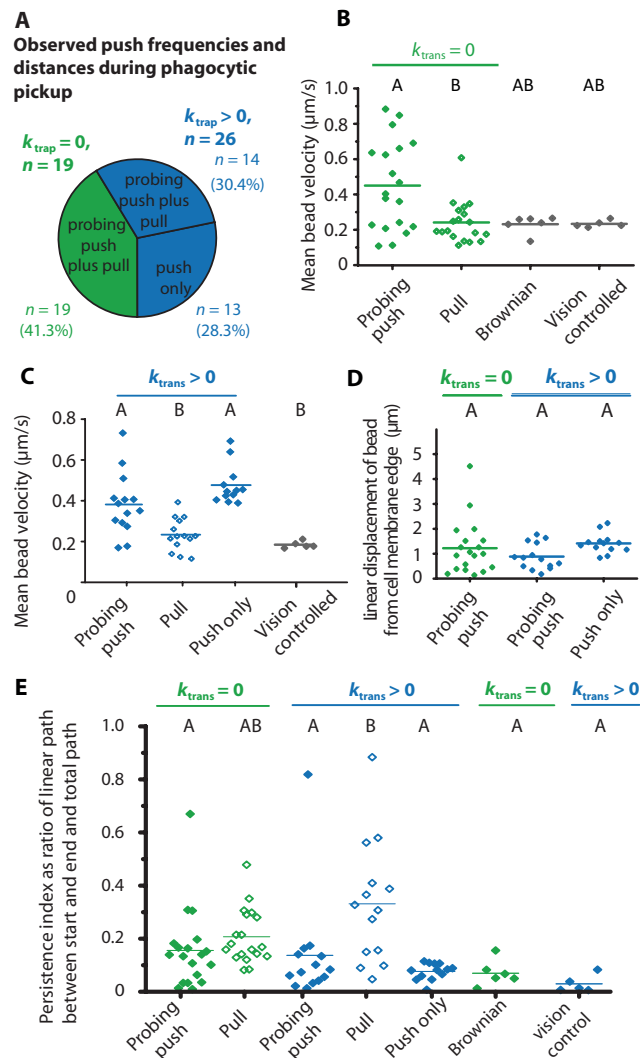


**Fig. 4. Quantification of pushing and pulling velocities, pushing forces, and persistence index analysis.** (A) Statistical analysis of recorded trajectories of spherical microparticles upon contact with macrophages, as shown in representative examples in Figs. 2, A to C, and 3. Two partitions were defined, that is, with a position-clamp stiffness of  $k_{\text{trans}} = 0$  (green) and  $k_{\text{trans}} > 0$  (blue). Two categories of pickup dynamics were determined: push with and without follow-up pull. (B) Cell-induced particle velocities differ from pure Brownian motion. Particle velocities were calculated by measuring the traveled distance over time at time intervals of 0.5 s. The measured velocities for beads under closed-loop clamp control using vision-based feedback are similar to velocities of free beads undergoing Brownian motion. A summary of  $n = 19$  experiments at a spring stiffness of  $k_{\text{trans}} = 0$  is shown. The variance of population means was analyzed using a one-way ANOVA. Uppercase letters mark significant differences based on post hoc Bonferroni test. Pairs of samples that have no letter in common have significantly different means at  $P < 0.05$ , that is, samples labeled A are significantly different from those labeled B. The mean linear push displacement in both cases and partitions is plotted on the left. The mean push deflection of the partition push only versus the mean probing push length of category “push with pull” is 1.6 times higher; however, no significant difference could be determined through a post hoc Bonferroni test. (C) Overview of the mean push and pull velocities for resistive prey, that is,  $k_{\text{trans}} > 0$ . Push velocities were similar in both cases, with and without follow-up pickup, and reflect the motion of the freely suspended bead. Upon contact, the velocity significantly dropped as the bead was pulled toward the cell body, reflecting the cell dynamics. (D) Linear displacement during measured push sequences of nonresistive and resistive prey. (E) Persistence of directionality as calculated by the ratio of linear displacement from original bead position to the total traveled path.

through binding but could also reflect a slowdown in the cellular process after successful contact and capture of the prey.

### Translational resistive prey is pushed less far

During pushing of nonresistive prey ( $k_{\text{trans}} = 0$ ), the mean linear particle displacement from its original position was  $1.2 \mu\text{m}$ , showing a substantial displacement away from the cell body (Fig. 4D). For resistive prey, the mean particle displacement during a push sequence without follow-up pull was 1.6 times higher than for cell events with follow-up pulling (mean displacement of  $1.4 \pm 0.4 \mu\text{m}$  versus  $0.9 \pm 0.5 \mu\text{m}$ ; Fig. 4D). The outward displacement indicates that actin protrusions grow toward the particle (24). A first contact can break or mature, and then trigger a reversal of the membrane position and bead direction, and thus shorten pushing distance.

Together, the applied forces did not hinder the particle transport toward the cell center once the macrophages had started to pull, as suggested by similar pulling velocities for  $k_{\text{trans}} = 0$  and  $k_{\text{trans}} > 0$ . Only in a few cases, the prey was pulled away from the cell by the applied magnetic forces in the range of 2 pN. However, small resistive counterforces during push sequences increased the initial efficiency by which particles were picked up by macrophages. This was indicated by the persistence of directionality, as calculated by the ratio of linear displacement from the original bead position to the total traveled path (Fig. 4E). Moreover, the persistence index was determined to be roughly twice as high in the cases of successful pickup at  $k_{\text{trans}} > 0$  (“push and pull”; mean persistence of pushes,  $0.14 \pm 0.2$ ), as opposed to unsuccessful particle pickup (push only; mean persistence of pushes,  $0.07 \pm 0.03$ ) (Fig. 4E). Likewise, the mean linear displacement of the push-only sequences at  $k_{\text{trans}} > 0$  indicated longer retention of the cell in a migratory mode while at similar velocity ranges, which agrees with a previous study on the migratory push by neutrophils (22). Together, initial pushing might ultimately increase the uptake rate because pushing, particularly against a counteracting force, might raise the probability of successful receptor-ligand bond formation.

### Rotational resistive prey impairs the pickup kinetics of macrophages

To release the pathogens from the surface, immune cells must break the surface adhesive bonds. Although we have observed earlier that non-

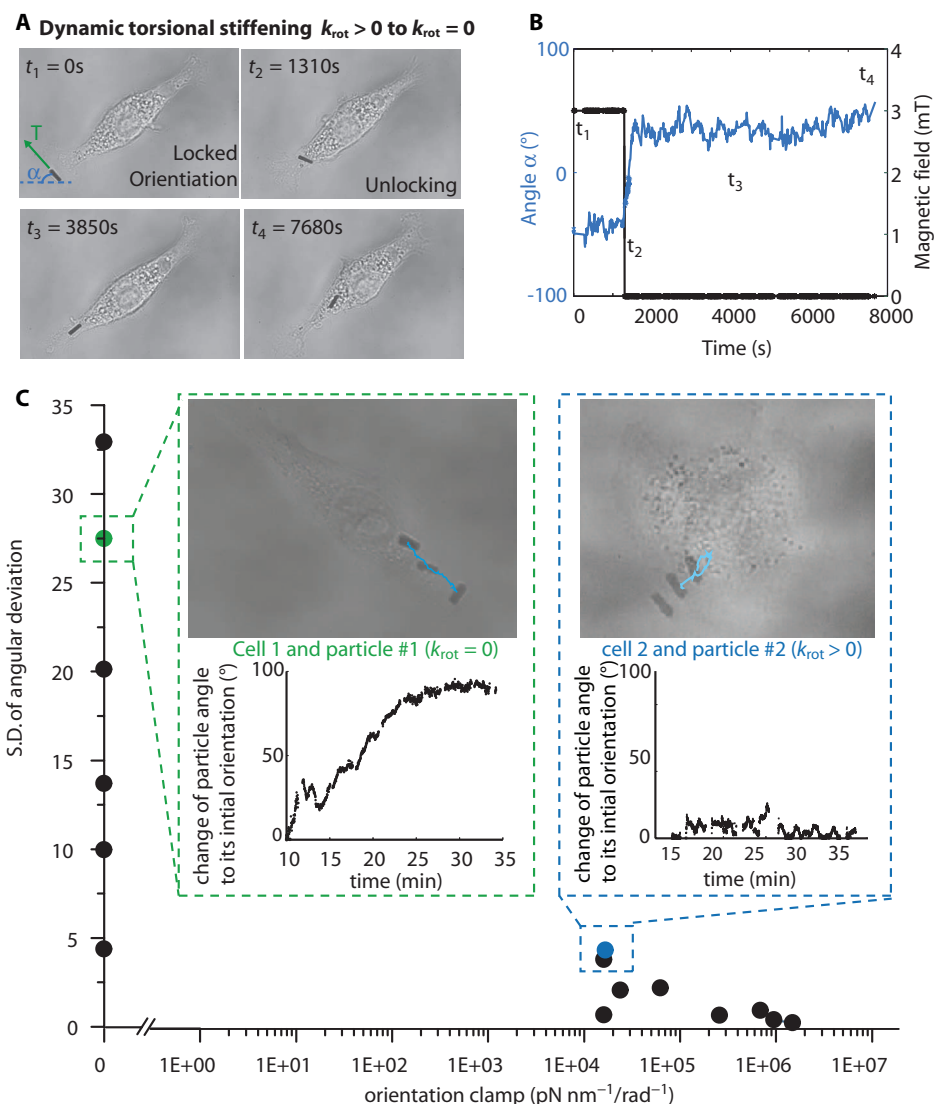


**Fig. 5. Rod-shaped microprey in combination with orientation clamp allows dynamic rotational control and quantification of torques applied by macrophages during particle pickup.** (A) Image sequence of a single cell confronted with rod-shaped prey in an initially locked orientation, followed by weakening of the orientation clamp and eventual complete release.

(B) Corresponding plot of the angle between the particle and its initial orientation during particle pickup under locked orientation, followed by weakening of the rotational resistance and subsequent change of orientation because of cellular pulling forces under unlocked conditions (that is, no externally applied magnetic torque, as seen from the magnetic field curve in black). (C) Summary of the interactions between macrophages and rod-shaped particles when impeded through the application of a torque clamp. The standard angular deviation is given with respect to its original angle. Green inset: One example of a macrophage picking up a freely rotatable particle. The change of particle angle over time is given as the difference to the initial particle angle and was calculated by subtracting the angle of the first time point from the angle of each subsequent time point. Blue inset: One example of a macrophage picking up a torque-clamped particle. Overview shows results of 15 experimental sequences in a large range of cell-opposing torques. Single data points represent time intervals with a defined torque. SD of the particle angle was reduced with increased applied torque.

resistive, elongated prey increased the rotational maneuvers of macrophages, we next wanted to investigate whether resistance to rotational maneuvers might affect the uptake kinetics. We therefore applied an impeding magnetic torque to maintain particle orientation during the cell-particle interaction. To decouple effects of rotational from translational resistance, only the orientation of the particle was locked, whereas the position was not restrained, that is, the cell could translate the particle without encountering a resistance. We followed the particle position and orientation over the duration of macrophage-particle interaction

and analyzed the SD of the particle angle. Altered pickup dynamics were detected compared with freely rotating rods (rotational stiffness  $k_{\text{rot}} = 0$ ) (Fig. 5). Rotationally locked rods were shuffled toward the cell body through the formation of large protrusions that formed underneath the rods (see also movie S8). Under a locked orientation at 6 mT, that is, applying a rotational stiffness  $k_{\text{rot}}$  on the order of  $2 \times 10^5$  pN nm rad $^{-1}$ , as determined by power density spectral fitting (text S4 and figs. S9 and S10), the orientation of the rod with respect to its original orientation fluctuated by only  $0.5 \pm 0.4^\circ$ . Upon weakening of the orientation clamp by reducing the externally applied magnetic field to 3 mT ( $k_{\text{rot}} = 1 \times 10^5$ ), a slight reorientation of the rod toward the cellular long axis was observed under increased motility with an angular change of  $3.9 \pm 4.96^\circ$ . When the orientation clamp was completely released, the rod was aligned parallel to the cell long axis within 8 min (Fig. 5, A and B), and a mean angular fluctuation of  $18.4 \pm 32.7^\circ$  of the rod to its initial orientation was measured during the course of the first 25 min after clamp release.

We evaluated 12 individual experiments with 15 experimental sequences and compared the SDs of the changing rod angle, as a measure of transport activity, of freely rotatable particles with those that had been rotationally clamped (Fig. 5C). In these 15 sequences, we consistently observed that the rotational transport maneuvers by the cells could be blocked by increasing the rotational resistance of the prey, as shown by the substantially reduced angular SD (Fig. 5C). Moreover, for high resistance ( $k_{\text{rot}} > 2 \times 10^5$  pN nm rad $^{-1}$ ), the prey that was initially aligned perpendicular to the cell long axis was not aligned with the cell axis unless the torque clamp was released. This suggests that the applied torques, which reduced or even fully stopped these rotational maneuvers, indicate the range of what a macrophage applies during prey maneuvering. This immediate stiffening response of the cells to changes in rotational resistance of the prey requires mechanosensing followed by fast cytoskeletal remodeling at the same time scale as previously reported in protrusion force experiments on macrophages (35).

Throughout pathogen phagocytosis, the contractile actomyosin cytoskeleton orchestrates the membrane dynamics and the applied cellular forces to the prey. To visualize filamentous actin in live cells, we transfected macrophages using the LifeAct-GFP expression system. We performed 11 time series of LifeAct-GFP imaging, in 7 of which we observed actin accumulation at the microrod contact point. The spatiotemporal trend of accumu-

lation along the microrod was visualized for one of the experiments in Fig. 6. Again, the particle position and orientation were recorded over the duration of the macrophage-particle interaction, and the deviation of the particle angle during cell encounter was analyzed (see also movie S9). The stiffness of the orientation clamp was altered by decreasing the magnetic field strength from 6 to 3 to 0 mT, that is, applying a rotational stiffness  $k_{\text{rot}}$  on the order of  $2 \times 10^5$ ,  $1 \times 10^5$ , and 0 pN nm rad $^{-1}$ , respectively. As observed in the experiments described earlier, the angular deviation as well as angular and translational velocity increased with decreasing rotational stiffness (Fig. 6, B to D). At a rotational stiffness on the order of  $k_{\text{rot}} > 2 \times 10^5$  pN nm rad $^{-1}$ ,

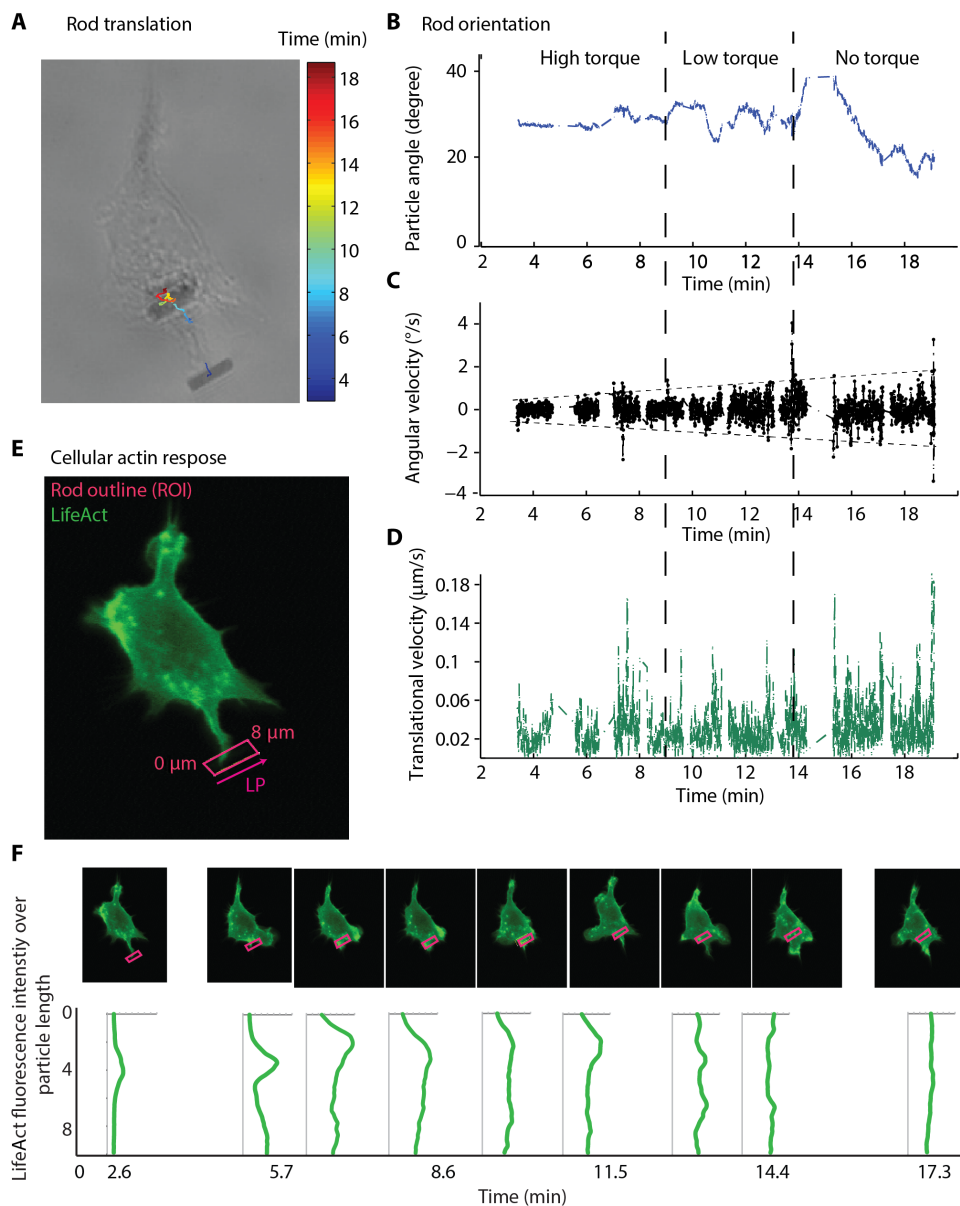


**Fig. 6. Macrophage attack of perpendicularly oriented particles and recruitment of actin to one of the particle poles.** (A) Trajectory of the particle over time overlaid with the cell outline. (B) The changes of the angle of the particle indicate rotations induced by the macrophage. By decreasing the rotational stiffness, the angular (C) and translational (D) velocities of the particle increase over time (see also movie S9). (E) LifeAct imaging of the cell was performed to visualize the F-actin cytoskeleton of the cells. The pink box indicates the region around the particle that was further analyzed in terms of its local actin activity. (F) The LifeAct signal under the area covered by the particle over time shows local actin recruitment and reinforcement of macrophage cytoskeleton to the particle.

the rods were not reoriented and an SD of  $\pm 4.5^\circ$  was measured (Fig. 6B). Upon release of the torque clamp, the reorientation of the long axis of the rods with the cellular axis was observed, resulting in an angular deviation of  $\pm 35.5^\circ$  within the first 5 min after the release and  $\pm 6^\circ$  after parallel alignment with the cellular long axis. After the initial push and pull of the rod toward the cell body, analysis of the LifeAct fluorescence intensity revealed that actin-rich regions formed at one pole of the rod. Formation of an actin-rich phagocytotic cup around the pole (27, 36) is a hallmark of initiating the internalization of nonspherical, high-aspect ratio prey (Fig. 6F) (13, 36).

Together, our quantitative observations of decreased reorientation activity when resisting the torque applied by macrophages to the prey agree with observations that phagocytosis of bacterial filaments and rod-shaped objects is impaired if the macrophages cannot reach their poles (12, 27, 36).

## DISCUSSION

Unconstrained control of nonresistive and resistive bacteria mimicking microparticles toward macrophages was demonstrated using a 5D-MTS that exploits optical displacement measurements of magnetic microparticles as feedback (Fig. 1). While monitoring particle and cell position, the dynamics of the cell-induced particle motion and the shape of the cells and other cellular features can be monitored on demand throughout the experiments. Arbitrarily shaped microparticles in the size range of bacteria were precisely positioned within three dimensions, and the forces and torques that macrophages exert when they attack their prey were studied (Figs. 2 to 6).

Distinct phases of the attack were identified (Figs. 2 to 4). Unexpectedly, macrophage attacks were often initiated by gentle pushing (Figs. 2 and 3). Gentle pushing was followed by a pull along a curved trajectory at velocities in the range of  $200 \pm 100 \text{ nm s}^{-1}$  and  $240 \pm 80 \text{ nm s}^{-1}$  for  $k_{\text{trans}} = 0$  and  $k_{\text{trans}} > 0$ , respectively (Fig. 4, B and C). We hypothesize that slight pushing may be required to increase the overall mechanical strength of the adhesive cell-prey contact because the formation of stable ligand-receptor interactions of the immune cells with their prey is a critical step in capturing and then engulfing the prey (24, 37, 38). The macrophages continued pushing the microprey over longer distances in those cases where they did not reverse into a pulling mode (Fig. 4D).

Although the necessity of nonspherical prey rotation in phagocytosis has been studied before (27–29, 36), we show here that rod-shaped particles can be locked in orientation by applying defined torques and that this does not interfere with their translation. We find that macrophages preferentially rotated elongated prey during pickup and that this range and rotation as well as velocity were consistently reduced by applied torques in the range of  $10^5 \text{ pN nm rad}^{-1}$  (Figs. 4, D and E; 5; and 6). For comparison, this stalling torque at which rotational maneuvers were blocked is about one to two orders of magnitude higher than torques exerted by motile bacteria, which have been reported to be in the range of 100 to 1000  $\text{pN nm rad}^{-1}$  (39, 40).

For low or nonresistive prey, rotational maneuvers by which the macrophages aligned the long axis of the particles with the main cellular axis were consistently observed and quantified (Figs. 2, C and D, 5, and 6). This alignment of the prey axis with the long cell axis was induced by actin accumulation at one end of the rod (Fig. 6F), supporting earlier findings of preferential attack of rod-like, nonspherical engineered particles and bacteria at their poles (27, 41). Taking our findings together, we report on a 5D-MTS that, combined with customized, arbitrary probes, enables advanced studies at the microscale

through dynamic probing of and interaction with complex processes in mechanobiology.

## MATERIALS AND METHODS

### Experimental setup

Our 5D-MTS generates arbitrary magnetic fields and field gradients up to 50 mT and  $5 \text{ T m}^{-1}$  at frequencies up to 2 kHz. It consists of eight electromagnets arranged in two inclined sets from the  $z$  axis, as described previously (text S1, “Specifications” section) (21, 42). The 5D-MTS was incorporated into an Olympus IX81 inverted microscope equipped with a fluorescent light source, a Point Grey Grasshopper GRAS-50S5C 15-fps FireWire camera, or a Basler scA1400 30-fps FireWire camera. We worked with a 40 $\times$  objective at  $\times 1.6$  additional magnification, resulting in a field of view of 1392 pixels  $\times$  1040 pixels at a pixel size of 101 nm. For real-time optical recording of the microparticle position, we used a modified shape detection algorithm to track the particle with subpixel resolution (43). Particles are stabilized with a mean deviation of 220 nm at room temperature (Fig. 1D and text S2). The magnetic forces were calculated on the basis of the calibrated applied magnetic fields and gradients and magnetic moment of the probe (see text S1, “Specifications,” “Magnetic control,” and “Calibration process” sections) (44). The trap stiffness was dynamically adjusted and could be set between  $k_{\text{trans,min}} = 0.7 \times 10^{-4} \text{ pN nm}^{-1}$  and  $k_{\text{trans,max}} = 1.8 \times 10^{-4} \text{ pN nm}^{-1}$ , which was calculated on the basis of the system calibration data. Stokes drag and fluctuation measurements were conducted to compare with the modeled data (see fig. S10). The linearity of the magnetic force with prey distance to the target was confirmed (see fig. S10). For the studies on rotational resistance, cobalt-nickel rods were used because of their shape anisotropy, and a rotational stiffness  $k_{\text{rot}}$  on the order of  $10^5 \text{ pN nm rad}^{-1}$  could be reached [see Fig. 1E, text S1 (“Magnetic control” section), and figs. S11 and S12].

### CoNi microprey fabrication

Magnetic microstructures were manufactured by 3D template-assisted electrodeposition (see fig. S1). The 3D templates were prepared by direct laser writing (Nanoscribe). Pulse electrodeposition was used to plate the magnetic cobalt-nickel microstructures. Cathodic pulses of 4 ms at a current density range of 50 to 100  $\text{mA cm}^{-2}$  and rest phases of 10 ms were used. The composition of the cobalt-nickel electrolyte and the electrodeposition conditions are given in table S1. The resulting microstructures were released from the template by removing the photoresist using acetone, isopropanol, and deionized (DI) water.

### Microprobe surface functionalization

Magnetic microspheres (Invitrogen Dynabeads M-450, tosylactivated) were functionalized via covalent coupling of the tosyl group on the Dynabeads to amine residues of purified *E. coli* type 1 fimbriae or of goat and mouse IgG against lipopolysaccharide (LPS) (Abcam ab35654). Our 3D-printed microrods were coated with a 50-nm layer of  $\text{SiO}_2$ . This layer was produced by plasma-enhanced chemical vapor deposition at 300 $^\circ\text{C}$  using  $\text{SiH}_4$  and  $\text{N}_2\text{O}$  as precursors. The resulting structures were collected by ultrasonication in DI water. The microrods were then coated with IgG molecules through adsorption over night and washed and suspended in phosphate-buffered saline before being added to the cells.

### Cell culture and imaging

Mouse macrophage-like cells (J774A.1 and RAW264.7) were cultivated in Dulbecco’s modified Eagle’s medium (Sigma D5921) supplemented with 10% fetal bovine serum (Biowest S181H), 25 mM Hepes (Biowest

L018), kanamycin ( $50 \mu\text{g ml}^{-1}$ ), and  $2.5 \text{ mM}$  L-glutamine. Twenty-four hours before magnetic measurements, cells were seeded at a density of  $20,000 \text{ cells cm}^{-2}$  in custom-made polydimethylsiloxane (PDMS) (Dow Corning Sylgard 184) wells with fibronectin-coated glass bottoms. To prime macrophages into M1 classically activated cells, we added interferon- $\gamma$  ( $2 \text{ ng ml}^{-1}$ ) and *E. coli* LPS (Sigma L4391  $100 \text{ ng/ml}$ ) 24 and 6 hours, respectively, before the measurements. Before imaging, macrophages were seeded on fibronectin-coated cover glasses within custom-made PDMS wells. Automated live cell imaging to monitor the interactions between freely rotatable or torque-clamped magnetic particles and RAW macrophages was performed in subsequent intervals of bright-field and fluorescence acquisition, using a  $40\times$  objective and a Nikon TE2000-E microscope, equipped with the Perfect Focus System.

### Statistical analysis

Descriptive statistics of mean values, SD, and one-way analysis of variance (ANOVA) tests of single-cell and population data were performed using the Origin 9.0 software (OriginLab). Statistical significance was estimated using the Tukey and Bonferroni tests at the specified thresholds.

### SUPPLEMENTARY MATERIALS

robotics.sciencemag.org/cgi/content/full/2/2/eaah6094/DC1

Text S1. The system

Text S2. Bead tracking: Brownian motion versus closed-loop control

Text S3. Dynamic position clamp

Text S4. Rotational trap stiffness modeling

Fig. S1. Schematic of microprey fabrication and SEM images.

Fig. S2. Macrophage attacking an elliptic prey.

Fig. S3. Macrophage encountering bowling pin-like prey.

Fig. S4. Image of 5D-MTS.

Fig. S5. SEM images of macrophages that phagocytosed rod-shaped prey.

Fig. S6. Overview of experimental categories.

Fig. S7. Velocity and force over time during push-pull sequence.

Fig. S8. Curved pickup trajectories.

Fig. S9. Velocity and force over time during push-only sequence.

Fig. S10. Position-clamp calibration.

Fig. S11. Torque calibration measurements.

Fig. S12. Torque evaluation.

Table S1. Electroplating conditions.

Movie S1. Control of rod-shaped prey toward a single macrophage.

Movie S2. Control of elliptic prey toward a single macrophage.

Movie S3. Nonresistive prey (raw video).

Movie S4. Nonresistive prey (postprocessed video).

Movie S5. Tracked cell with nonresistive rod-shaped prey.

Movie S6. Realignment of nonresistive rod-shaped prey.

Movie S7. "Push-pull" maneuver of a macrophage.

Movie S8. Macrophage maneuver with dynamically resistive prey.

Movie S9. Macrophage maneuver with dynamically resistive prey combined with LifeAct-GFP imaging.

### REFERENCES AND NOTES

- W. W. Murdoch, A. Oaten, Predation and population stability, in *Advances in Ecological Research*, A. MacFadyen, Ed. (Academic Press, 1975), vol. 9, pp. 1–31.
- I. Schoen, B. L. Pruitt, V. Vogel, The yin-yang of rigidity sensing: How forces and mechanical properties regulate the cellular response to materials. *Annu. Rev. Mater. Res.* **43**, 589–618 (2013).
- V. Vogel, M. Sheetz, Local force and geometry sensing regulate cell functions. *Nat. Rev. Mol. Cell Biol.* **7**, 265–275 (2006).
- J. L. Tan, J. Tien, D. M. Pirone, D. S. Gray, K. Bhadriraju, C. S. Chen, Cells lying on a bed of microneedles: An approach to isolate mechanical force. *Proc. Natl. Acad. Sci. U.S.A.* **100**, 1484–1489 (2003).
- N. Leijnse, L. B. Oddershede, P. M. Bendix, An updated look at actin dynamics in filopodia. *Cytoskeleton* **72**, 71–79 (2015).
- T. Bornschlög, How filopodia pull: What we know about the mechanics and dynamics of filopodia. *Cytoskeleton* **70**, 590–603 (2013).
- R. S. Flannagan, V. Jaumouillé, S. Grinstein, The cell biology of phagocytosis. *Annu. Rev. Pathol.* **7**, 61–98 (2012).
- K. C. Neuman, A. Nagy, Single-molecule force spectroscopy: Optical tweezers, magnetic tweezers and atomic force microscopy. *Nat. Methods* **5**, 491–505 (2008).
- J. Castillo, M. Dimaki, W. E. Svendsen, Manipulation of biological samples using micro and nano techniques. *Integr. Biol.* **1**, 30–42 (2009).
- Z. Yan, M. Pelton, L. Vigderman, E. R. Zubarev, N. F. Scherer, Why single-beam optical tweezers trap gold nanowires in three dimensions. *ACS Nano* **7**, 8794–8800 (2013).
- J. Lipfert, J. W. J. Kerssemakers, T. Jager, N. H. Dekker, Magnetic torque tweezers: Measuring torsional stiffness in DNA and RecA-DNA filaments. *Nat. Methods* **7**, 977–980 (2010).
- J. A. Champion, S. Mitragotri, Role of target geometry in phagocytosis. *Proc. Natl. Acad. Sci. U.S.A.* **103**, 4930–4934 (2006).
- A. Prashar, S. Bhatia, D. Gigliozzi, T. Martin, C. Duncan, C. Guyard, M. R. Terebiznik, Filamentous morphology of bacteria delays the timing of phagosome morphogenesis in macrophages. *J. Cell Biol.* **203**, 1081–1097 (2013).
- J. Lipfert, M. Lee, O. Ordu, J. W. J. Kerssemakers, N. H. Dekker, Magnetic tweezers for the measurement of twist and torque. *J. Vis. Exp.* **2014**, e51503 (2014).
- A. La Porta, M. D. Wang, Optical torque wrench: Angular trapping, rotation, and torque detection of quartz microparticles. *Phys. Rev. Lett.* **92**, 190801 (2004).
- C. Deufel, S. Forth, C. R. Simmons, S. Dejgosh, M. D. Wang, Nanofabricated quartz cylinders for angular trapping: DNA supercoiling torque detection. *Nat. Methods* **4**, 223–225 (2007).
- F. Pedaci, Z. Huang, M. van Oene, S. Barland, N. H. Dekker, Excitable particles in an optical torque wrench. *Nat. Phys.* **7**, 259–264 (2011).
- Y. Seol, K. C. Neuman, SnapShot: Force spectroscopy and single-molecule manipulation. *Cell* **153**, 1168–1168.e1 (2013).
- P. Stoodley, K. Sauer, D. G. Davies, J. W. Costerton, Biofilms as complex differentiated communities. *Annu. Rev. Microbiol.* **56**, 187–209 (2002).
- S. Schuerle, M. S. Sakar, A. Meo, J. Möller, B. E. Kratochvil, C. S. Chen, V. Vogel, B. J. Nelson, Three-dimensional, automated magnetic biomanipulation with subcellular resolution, paper presented at the 2013 IEEE International Conference on Robotics and Automation (ICRA 2013), Karlsruhe, Germany, 6 to 10 May 2013.
- S. Schuerle, S. Erni, M. Flink, B. E. Kratochvil, B. J. Nelson, Three-dimensional magnetic manipulation of micro- and nanostructures for applications in life sciences. *IEEE Trans. Magn.* **49**, 321–330 (2013).
- M. Herant, C.-Y. Lee, M. Dembo, V. Heinrich, Protrusive push versus enveloping embrace: Computational model of phagocytosis predicts key regulatory role of cytoskeletal membrane anchors. *PLOS Comput. Biol.* **7**, e1001068 (2011).
- D. Choquet, D. P. Felsenfeld, M. P. Sheetz, Extracellular matrix rigidity causes strengthening of integrin-cytoskeleton linkages. *Cell* **88**, 39–48 (1997).
- R. S. Flannagan, R. E. Harrison, C. M. Yip, K. Jaqaman, S. Grinstein, Dynamic macrophage "probing" is required for the efficient capture of phagocytic targets. *J. Cell Biol.* **191**, 1205–1218 (2010).
- V. Jaumouillé, Y. Farkash, K. Jaqaman, R. Das, C. A. Lowell, S. Grinstein, Actin cytoskeleton reorganization by Syk regulates Fc $\gamma$  receptor responsiveness by increasing its lateral mobility and clustering. *Dev. Cell* **29**, 534–546 (2014).
- H. Kress, E. H. K. Stelzer, D. Holzer, F. Buss, G. Griffiths, A. Rohrbach, Filopodia act as phagocytic tentacles and pull with discrete steps and a load-dependent velocity. *Proc. Natl. Acad. Sci. U.S.A.* **104**, 11633–11638 (2007).
- J. Möller, T. Luehmann, H. Hall, V. Vogel, The race to the pole: How high-aspect ratio shape and heterogeneous environments limit phagocytosis of filamentous *Escherichia coli* bacteria by macrophages. *Nano Lett.* **12**, 2901–2905 (2012).
- J. Wang, J. D. Byrne, M. E. Napier, J. M. DeSimone, More effective nanomedicines through particle design. *Small* **7**, 1919–1931 (2011).
- N. Doshi, S. Mitragotri, Designer biomaterials for nanomedicine. *Adv. Funct. Mater.* **19**, 3843–3854 (2009).
- J. Li, G. Du, Manipulation and assembly of ZnO nanowires with single holographic optical tweezers system. *Appl. Optics* **53**, 351–355 (2014).
- Z. Yan, J. E. Jureller, J. Sweet, M. J. Guffey, M. Pelton, N. F. Scherer, Three-dimensional optical trapping and manipulation of single silver nanowires. *Nano Lett.* **12**, 5155–5161 (2012).
- T. Bornschlög, S. Romero, C. L. Vestergaard, J.-F. Joanny, G. T. Van Nhieu, P. Bassereau, Filopodial retraction force is generated by cortical actin dynamics and controlled by reversible tethering at the tip. *Proc. Natl. Acad. Sci. U.S.A.* **110**, 18928–18933 (2013).
- J.-S. Shin, S. N. Abraham, Glycosylphosphatidylinositol-anchored receptor-mediated bacterial endocytosis. *FEMS Microbiol. Lett.* **197**, 131–138 (2001).
- J. Möller, T. Luehmann, M. Chabria, H. Hall, V. Vogel, Macrophages lift off surface-bound bacteria using a filopodium-lamellipodium hook-and-shovel mechanism. *Sci. Rep.* **3**, 2884 (2013).
- A. Labernadie, A. Bouissou, P. Delobelle, S. Balor, R. Voituriez, A. Proag, I. Fourquaux, C. Thibault, C. Vieu, R. Poincloux, G. M. Charrière, I. Maridonneau-Parini, Protrusion

- force microscopy reveals oscillatory force generation and mechanosensing activity of human macrophage podosomes. *Nat. Commun.* **5**, 5343 (2014).
36. J. A. Champion, S. Mitragotri, Shape induced inhibition of phagocytosis of polymer particles. *Pharm. Res.* **26**, 244–249 (2009).
  37. W. L. Lee, D. Mason, A. D. Schreiber, S. Grinstein, Quantitative analysis of membrane remodeling at the phagocytic cup. *Mol. Biol. Cell* **18**, 2883–2892 (2007).
  38. J. A. Swanson, Shaping cups into phagosomes and macropinosomes. *Nat. Rev. Mol. Cell Biol.* **9**, 639–649 (2008).
  39. Y. Hyon, Marcos, T. R. Powers, R. Stocker, H. C. Fu, The wiggling trajectories of bacteria. *J. Fluid Mech.* **705**, 58–76 (2012).
  40. S. M. Block, D. F. Blair, H. C. Berg, Compliance of bacterial flagella measured with optical tweezers. *Nature* **338**, 514–518 (1989).
  41. S. Mitragotri, J. Lahann, Physical approaches to biomaterial design. *Nat. Mater.* **8**, 15–23 (2009).
  42. M. P. Kummer, J. Abbott, B. Kratochvil, R. Borer, A. Sengul, B. Nelson, OctoMag: An electromagnetic system for 5-DOF wireless micromanipulation. *IEEE Trans. Robot.* **26**, 1006–1017 (2011).
  43. B. E. Kratochvil, L. Dong, B. J. Nelson, Real-time rigid-body visual tracking in a scanning electron microscope. *Int. J. Rob. Res.* **28**, 498–511 (2009).
  44. G. Fonnum, C. Johansson, A. Molteberg, S. Mørup, E. Aksnes, Characterisation of Dynabeads® by magnetization measurements and Mössbauer spectroscopy. *J. Magn. Mater.* **293**, 41–47 (2005).
- on cell contour tracking, and P. Kollmansberger for discussions of the manuscript.
- Funding:** We acknowledge financial support from ETH Zürich, the Swiss National Competence Center of Research (NCCR) Molecular Systems Engineering to V.V., and the Commission of the European Communities/European Research Council (ERC) Advanced Grants (grant 231157 to V.V. and grant 268004 BOTMED to B.J.N.). S.P. and F.M. acknowledge financial support by the ERC Starting Grant “Magnetolectric Chemonanorobotics for Chemical and Biomedical Applications (ELECTROCHEMBOTS)” (ERC grant agreement number 336456). S.S. acknowledges the support by the Swiss National Science Foundation (SNSF) through the “Early Postdoc Mobility Fellowship” and funding provided by the DAAD, German Academic Exchange Service. **Author contributions:** S.S. and I.A.V. performed experiments and analyzed and interpreted data, and S.S., I.A.V., J.M., B.J.N., and V.V. wrote the paper. S.S. implemented the 5D and MTS and wrote the data analysis scripts. J.M. and S.S. performed the very initial experiments. S.S., I.A.V., J.M., M.S.S., B.J.N., and V.V. designed the research. B.Ö., A.M.L., S.P., and F.M. fabricated the microparticles. S.S. and I.S. performed the torque calibrations. All authors read and commented on the manuscript. **Competing interests:** The authors declare that they have no competing interests.

Submitted 20 July 2016

Accepted 8 December 2016

Published 4 January 2017

10.1126/scirobotics.aah6094

**Citation:** S. Schuerle, I. A. Vizcarra, J. Moeller, M. S. Sakar, B. Özkale, A. M. Lindo, F. Mushtaq, I. Schoen, S. Pané, V. Vogel, B. J. Nelson, Robotically controlled microprey to resolve initial attack modes preceding phagocytosis. *Sci. Robot.* **2**, eaah6094 (2017).

**Acknowledgments:** We thank B. Kratochvil for the implementation of the Canny edge detection algorithm for real-time particle tracking, M. Dätwiler and R. Pieters for contributions